Different aggregation states of a nuclear localization signal-tagged 25 kDa C-terminal fragment of TAR RNA/DNA-binding protein 43 kDa

Akira Kitamura[1], **Sachiko Yuno**[1], **Hideki Muto**[1,#], **Masataka Kinjo**[1,*]

[1] Laboratory of Molecular Cell Dynamics, Faculty of Advanced Life Science, Hokkaido University, Sapporo, Japan

[#] Current address: Biomedical Research Support Center, Nagasaki University School of Medicine, Nagasaki, Japan

* Corresponding author

E-mail: kinjo@sci.hokudai.ac.jp

Abstract

The mechanism and cause of motor neuronal cell death in amyotrophic lateral sclerosis (ALS), a devastating neurodegenerative disorder, is unknown, gain-of-function of oligomers and aggregation of misfolded proteins, including carboxyl-terminal fragments (CTFs) of TAR RNA/DNA-binding protein 43 kDa (TDP-43) have been proposed as important causative factors in the onset of ALS. We recently reported that a nuclear localization signal (NLS)-tagged 25-kDa CTF of TDP-43 (TDP25) could decrease the cell-death proportion compared with that promoted by TDP25. Here, we show that oligomeric states of NLS-TDP25 and its detailed localization property using super-resolution fluorescence microscopy, FRET, fluorescence recovery after photobleaching, and fluorescence correlation spectroscopy analysis. NLS-TDP25 efficiently formed a nucleolar cap structure *via* RNA-binding in presence of actinomycin D, but TDP25 did not. Although cytoplasmic inclusion bodies (IBs) including TDP25 had a disordered and immobile structure, NLS-TDP25 in the nucleolus was ordered and dynamic. In the diffuse state, TDP25 formed fewer oligomers and interacted with the molecular chaperone, HSP70; however, NLS-TDP25 formed oligomers. These results suggested that NLS-tagged TDP25 can change its structure to adopt ordered oligomeric but non-toxic state. Moreover, the structure of ordered oligomers as well as nuclear sequestration may be important in mediating cytotoxicity in ALS-pathology.

Introduction

Amyotrophic lateral sclerosis (ALS) is a neurodegenerative disease characterized by dysfunctional motor neurons and muscle atrophy, inclusion bodies (IBs) containing protein aggregates, and the formation of RNA-protein complexes in the cytoplasm and nucleus of motor neurons (Neumann *et al.* 2006; Blokhuis *et al.* 2013). These IBs are ubiquitin (Ub)-positive and often contain proteins encoded by ALS-causative genes, including superoxide dismutase 1 (SOD1), *TARDBP* (TDP-43), fused in Sarcoma/translocated in Sarcoma (FUS/TLS), *OPTN* (Optineurin), among others (Renton *et al.* 2014). Typically, ALS-associated proteins are prone to aggregate and adopt misfolded and/or prion-like properties (Gitler & Shorter 2011).

TDP-43 is the major disease-associated protein of ALS and frontotemporal lobar degeneration associated with TDP-43 (FTLD-TDP). TDP-43 carries 2 RNA/DNA-recognition motifs (RRM1 and RRM2) and a C-terminal glycine-rich region (GRR) including the prion-like Q/N-rich domain (also

known as *the low-complexity sequence domain*). The consensus RNA/DNA sequence recognized by the RRM is known to be UG/TG repeats (Kuo *et al.* 2009; Lukavsky *et al.* 2013). The GRR mediates interactions with heterogeneous ribonucleoproteins (hnRNPs) (D'Ambrogio *et al.* 2009). TDP-43 harbors a classical nuclear localization signal (NLS) between the N-terminal Ub-like domain and RRM1, as well as a nuclear export signal (NES) in RRM2 (Blokhuis *et al.* 2013). Thus, TDP-43 is subject to nuclear-cytoplasmic shuttling and mediates RNA-associated functions, mRNA splicing, microRNA processing, and mRNA transport to the cytoplasm.

It has been shown that not only intact TDP-43 but also several CTFs of TDP-43 are incorporated into cytoplasmic IBs (Neumann *et al.* 2006; Fung *et al.* 2015). The 25-kDa TDP-43 CTF (TDP-$43_{220–414}$) is also known as TDP25 (Zhang *et al.* 2009). TDP25 can be generated by caspase 3- and/or calpain-dependent cleavage of intact TDP-43 (Zhang *et al.* 2007; Yamashita *et al.* 2012). TDP25 lacks an NLS, RRM1, and a portion of RRM2. Therefore, TDP25 does not recognize RNA/DNA that can be recognized by TDP-43 and is distributed in the nucleus and cytoplasm (Kitamura *et al.* 2016). TDP25 is prone to aggregation and forming Ub-positive IBs in the cytoplasm. Recently, we reported that NLS-tagged TDP25 (NLS-TDP25) shows less cytotoxicity than TDP25 and does not become incorporated into cytoplasmic IBs (Kitamura *et al.* 2016). In addition, cytoplasmic aggregation of a CTF of TDP-43 interferes with nuclear-cytoplasmic transport by altering the subcellular deposition of transport-associated proteins (Woerner *et al.* 2016). These findings suggested that the cytoplasmic existence of misfolded aggregation-prone proteins including TDP-43 CTF may lead to neuronal cell death by causing dysfunction in cellular proteostasis.

It is known that cytoplasmic molecular chaperones including heat shock protein 70 kDa, 90 kDa, and 40 kDa (HSP70, HSP90, and HSP40, respectively) play a critical role to prevent aggregation of misfolded protein (Morimoto 2008; Brehme *et al.* 2014). Induction of these cytoplasmic molecular chaperones in cultured cells by heat shock decreased aggregation of TDP-43 CTFs (Udan-Johns *et al.* 2014; Chen *et al.* 2016). Since an inhibitor of HSP70 ATPase activity during inhibition of proteasome activity increased insoluble TDP-43 and its CTF, HSP70 is known as a major contributor to TDP-43 proteostasis (Lin *et al.* 2016).

However, it remains unclear how NLS-TDP25 evades cytoplasmic aggregation and IB formation. It is important to clarify the mechanism of inhibited aggregation, which is involved in neuronal cell death, in order to understand ALS pathophysiology and develop a strategy for curing ALS. Therefore,

we analyzed the detailed molecular properties of NLS-TDP25 and TDP25 using multiple biophysical fluorescence spectroscopic techniques, including Förster/fluorescence energy transfer (FRET), fluorescence recovery after photobleaching (FRAP), and fluorescence correlation spectroscopy (FCS).

Results

Nucleolar localization property of TDP25 in inhibiting proteasomal and RNA-transcriptional activity. In cells carrying no cytoplasmic IBs, GFP-tagged TDP25 (G-TDP25) was observed in the cytoplasm and nucleoplasm, but not in the nucleolus (Fig. 1A). This reduction in nucleolar localization was also seen with TDP-43 tagged with GFP (TDP43-G; Fig. 1A). In contrast, TDP25 fused to GFP and the SV40 virus-derived NLS peptide that can bind to RNA including UG-repeat (G-NLS-TDP25) localized into the nucleolus and nucleoplasm (Fig. 1A), as previously reported (Kitamura *et al.* 2016). Localization of G-NLS-TDP25 was enriched in the boundary region between the nucleolus and nucleoplasm (Fig. 1B). The nucleolar localization property of G-NLS-TDP25 is thought to be involved in the RNA-binding property of the NLS tag, because TDP25 fused to GFP and nucleoplasmin-derived NLS peptide that does not bind to UG-repeat RNA (G-NLS^{NP}-TDP25) was not localized in the nucleolus (Kitamura *et al.* 2015b; Kitamura *et al.* 2016); thus, we examined whether the nucleolar localization of G-NLS-TDP25 could be affected by inhibiting RNA transcription using actinomycin D (ActD). Following ActD treatment, the localization of G-NLS-TDP25 was altered and formed nucleolar cap-like structures and foci in the nucleoplasm. TDP43-G similarly formed nucleolar cap-like structures following ActD treatment (Fig. 1, C & D; Fig. S1). In contrast, nucleolar cap-like structures of NLS-tagged GFP (G-NLS), which served as a negative control, were not formed after ActD treatment (Fig. 1, C & D; Fig. S1). In addition, G-TDP25 and G-NLS^{NP}-TDP25 did not form nucleolar cap-like structure after ActD treatment (Fig. 1, C & D; Fig. S1). This finding suggested that both C-terminal glycine rich region of TDP-43 and UG-repeat RNA-binding property are likely required for the state of nucleolar cap-like structure of TDP-43 during inhibition of RNA transcription.

Next, we observed the localization pattern of G-NLS-TDP25 during the inhibition of proteasome activity as a state of dysregulation of proteostasis and accumulation of misfolded proteins. Interestingly, G-NLS-TDP25 accumulation in the boundary region between the nucleolus and nucleoplasm significantly increased following inhibition of proteasome activity, whereas G-NLS as a tag was not (Fig. 1, E & F). This result may reflect a mechanism of sequestration of an aggregation-prone protein

in the nucleolus during the dysregulation of proteostasis.

Exchange dynamics of G-NLS-TDP25 between the nucleolus and nucleoplasm. To determine the exchange rate of G-NLS-TDP25 between the nucleolus and nucleoplasm, we performed FRAP analysis of G-NLS-TDP25 (Fig. 2A). The fluorescence-recovery proportion of G-NLS-TDP25 in the nucleolus was 53.6% without proteasome inhibition, but proteasome inhibition significantly decreased in the mobile fraction (to 8.9%; Fig. 2A). G-NLS in the nucleolus (measured as a control) showed rapid recovery and more than 97% mobility, both with and without proteasome inhibition (Fig. 2B). The 53.6% mobility of G-NLS-TDP25 in the nucleolus without proteasome inhibition strongly contrasted with the previously shown 11% mobility of G-TDP25 in cytoplasmic IBs (Kitamura *et al.* 2016). The increased immobility and efficient formation of nucleolar boundary structure of NLS-TDP25 in presence of MG-132 suggested that nucleolar accumulation of G-NLS-TDP25 may not involve sequestration by other proteins, but may be due to a signal promoting the nucleolar retention of G-NLS-TDP25 that shows increased activity during proteasome inhibition.

Distinct intermolecular orientation of NLS-TDP25. Next, we investigated how NLS-TDP25 accumulated in the nucleolus. To compare the intermolecular orientation of TDP25 in cytoplasmic IBs and during nucleolar accumulation, we performed intermolecular FRET analysis between TDP25 or NLS-TDP25 N-terminally fused to monomeric super-enhanced cyan fluorescent protein (mSECFP) as a donor and a monomeric and bright variant of yellow fluorescent protein (mVenus) as an acceptor. We recently reported that the intermolecular orientation of an aggregation-prone protein in IBs could be determined by comparing the FRET efficiency between a conventional fluorescent protein and a circular permutant (CP) as an acceptor (Kitamura *et al.* 2014; Kitamura *et al.* 2015a). Thus, we employed a CP variant of mVenus (cp173mVenus) in this study. In cytoplasmic IBs, the FRET efficiency of TDP25 was not affected by changing the orientation of the acceptor (Fig. 3A, lanes 1 and 2), indicating that TDP25 is present in accumulated cytoplasmic IBs in an angle-independent orientation in an amorphous state. In contrast, the FRET efficiency of NLS-TDP25 in the nucleolus was significantly changed by introduction of the tagged CP variant (48% and 33%; Fig. 3A, lanes 3 and 4, respectively) and was significantly higher than that of a non-FRET control (5.0% and 1.8%; Fig. 3A, lanes 5 and 6, respectively). Next, to check a different conformation of TDP-25 itself rather than an effect of NLS, we

further analyzed intermolecular FRET of NLS-TDP25 fused to C-terminal fluorescent tags. The FRET efficiency was significantly affected by changing the orientation of the acceptor (4.1% and 9.9%; Fig. 3B). These findings indicated that the intermolecular orientation of NLS-TDP25 in the nucleolus was ordered and completely different from that of TDP25 in the cytoplasmic IBs.

Next, we analyzed the FRET efficiency of a non-IB-forming region of TDP25 in the nucleoplasm and cytoplasm (Fig. 3C, lanes 1–4). Positive FRET efficiency of TDP25 in the cytoplasm and nucleoplasm was not observed, either in the presence or absence of the tagged CP (Fig. 3C, lanes 1-4). In contrast, nucleoplasmic NLS-TDP25 showed weak but significantly positive FRET efficiency compared to that observed with co-expression of a monomeric donor and acceptor as a negative control (Fig. 3C, lanes 5 and 6), suggesting that a portion of NLS-TDP25 may form oligomers in the nucleoplasm. These results suggested that the intermolecular orientation of NLS-TDP25 was completely different from that of TDP25.

Molecular diffusion dynamics of TDP25 and NLS-TDP25. Next, to analyze whether the negative FRET efficiency of TDP25 in the nucleoplasm and the cytoplasm reflected reduced oligomerization, we analyzed the diffusion state of G-TDP25 in live cells using FCS, which can detect molecular dynamics and oligomeric states with single-molecule sensitivity (Rigler *et al.* 1993; Kitamura *et al.* 2006; Kitamura *et al.* 2015b). G-TDP25 and G-NLS-TDP25 were slowly diffuse compare with monomeric GFP in the live cells (Fig. S2). We performed curve-fitting analysis using a 1- or 2-component diffusion model for GFP in the nucleolus or others, respectively. Fitting with the 2-component diffusion model for GFP in the nucleolus did not show slow component; thus, diffusion coefficient of GFP in the nucleolus obtained from fitting with the 1-component model was categorized as the fast diffusion. The fast-diffusion coefficients (D_{Fast}) of G-TDP25, G-NLS-TDP25, and G-NLS in the nucleoplasm or cytoplasm were significantly smaller than those of GFP in the same compartments, which were studied as controls The estimated molecular weights from the D_{Fast} values for G-TDP25 and G-NLS-TDP25 were 100–200 kDa, indicating that G-TDP25 and G-NLS-TDP25 were not present as monomers in the cytoplasm and nucleoplasm. (Fig. 4A). Although the D_{Fast} of G-NLS-TDP25 in the nucleoplasm (17.2 ± 7.61 $\mu m^2/s$) was not different from that of the G-NLS control (23.7 ± 12.9 $\mu m^2/s$), the slow-diffusion coefficient (D_{Slow}) of G-NLS-TDP25 in the nucleoplasm (0.943 ± 0.537 $\mu m^2/s$) was significantly smaller than that of G-NLS (2.75 ± 2.36 $\mu m^2/s$; Fig. 4B), indicating that the molecular

weight of slowly diffusing complexes including G-NLS-TDP25 was higher than those including G-NLS. The slowly diffuse component of G-TDP25 in any compartments and G-NLS-TDP25 in the nucleoplasm increased significantly compared to that of GFP (Fig. 4C). These results suggested that G-TDP25 and G-NLS-TDP25 formed oligomers and/or complexes with endogenous proteins in the live cells, but unfortunately, we did not distinguish diffusion property between G-TDP25 and G-NLS-TDP25. Next, we analyzed the counts per molecule (CPM) value, which indicates molecular fluorescence brightness per single particle measured by FCS analysis, detecting homo-oligomerization of fluorescent molecules. The CPM values of both G-TDP25 and G-NLS-TDP25 were smaller than that of the GFP control, suggesting that their fluorescence-emission efficiencies were likely lower than that of monomeric GFP in live cells (Fig. 4D); therefore, we could not directly investigate the existence of homo-oligomers of G-TDP25 and G-NLS-TDP25 by using the CPM analysis. However, the intermolecular FRET efficiency of NLS-TDP25 was positive in the nucleoplasm (Fig. 3B); therefore, at least NLS-TDP25 forms homo-oligomers in the nucleoplasm, whereas TDP25 forms high molecular weight complex with endogenous partner-proteins likely rather than homo-oligomers.

Although both the D_{Fast} and D_{Slow} values of G-TDP25 in the nucleolus were not different from those in the cytoplasm and nucleoplasm, the fraction of slow component increased compared to that in the cytoplasm and nucleoplasm (Fig. 4C), indicating that a portion of G-TDP25 can localize to the nucleolus and diffuses slowly.

Our FRET and FCS analyses revealed that NLS-TDP25 forms oligomers and diffuses in the nucleoplasm, while TDP25 also diffuses in the nucleoplasm, but forms fewer oligomers. The oligomerization of NLS-TDP25 may serve an important role in preventing the transmission of aggregation and may be involved in inhibiting the formation of cytoplasmic IBs.

TDP25 and NLS-TDP25 binds to the molecular chaperone, HSP70. To identify endogenous interacting-partner proteins with TDP25, we performed IP of G-TDP25 followed by MS was performed. After IP of G-TDP25 using an anti-GFP antibody, several G-TDP25-specific bands were obtained (Fig. 5A). The bands (ii) and (iii) of Fig. 5A were determined to be TDP-43 by MS. Thus, these bands (ii & iii) were G-TDP25. Band (i) was identified as heat shock protein family A member 8 (HSPA8), a cognate type of HSP70, which is a cytoplasmic and nuclear molecular chaperone carrying a substrate-release function in the presence of adenosine triphosphate (ATP) (Morimoto 2008; Kampinga & Craig

2010; Hartl *et al.* 2011). Band (iv) in the negative-control GFP lane was detected as GFP. These results indicated that HSP70 was specifically co-precipitated with G-TDP25.

Next, to confirm the interaction between G-TDP25 and HSP70 in a soluble state, we performed fluorescence cross-correlation spectroscopy (FCCS) analysis, which can detect interactions between 2-color fluorescent molecules in solution with single-molecule sensitivity (Bacia *et al.* 2006; Kitamura *et al.* 2016). A positive and high amplitude of the cross-correlation function (CCF) was found between G-TDP25 and RFP-tagged HSP70 (HSP70-R) in the cell lysate (blue line in Fig. 5B). In contrast, addition of magnesium ion and ATP to the cell lysate decreased the CCF amplitude (magenta line in Fig. 5B). Moreover, weaker CCF amplitudes between GFP and RFP were observed in the presence or absence of magnesium ion and ATP (orange and green lines in Fig. 5B). These results indicated that HSP70 may transiently bind to TDP25 with its ATPase cycle.

Next, to compare HSP70-interaction state between TDP25 and NLS-TDP25, we performed immunoprecipitation followed by western blotting. Lysates of Neuro2A cells expressing GFP, G-NLS, G-TDP25, or G-NLS-TDP25 were prepared, and immunoprecipitation was performed using anti-GFP antibody-conjugated beads. Endogenous HSPA8 was co-precipitated with G-TDP25 and G-NLS-TDP25, but not with GFP and G-NLS as tags (Fig. 5C). The band intensity of co-precipitated HSPA8 with G-NLS-TDP25 was not changed compared to that with G-TDP25, suggesting that both G-TDP25 and G-NLS-TDP25 in a soluble state are likely recognized by HSP70 at a similar level (Fig. 5C, lanes 3 & 4).

Next, confocal fluorescence microscopy revealed that fluorescence intensity of HSP70-R in a cytoplasmic inclusion body of G-TDP25 was high, whereas that of HSP70-R in the nucleolus accumulating G-NLS-TDP25 was low (Fig. 5D). The co-localization of RFP as a tag with G-TDP25 in the cytoplasmic inclusion body and with G-NLS-TDP25 in the nucleolus was not observed (Fig. 5D). In addition, HSP70-R and RFP was not accumulated in the nucleolus in cells expressing TDP43-G, G-NLS, and GFP (Fig. 5D and Fig. S3). It was suggested that HSP70 can bind to both TDP25 and NLS-TDP25; however, HSP70 may strongly bind to disordered aggregation of TDP25. Since HSP70 is known as a molecular chaperone recognizing denatured substrates preferentially, these results suggested that HSP70 interacted to G-TDP25 and NLS-TDP25 likely due to protect aggregation formation.

Discussion

Our findings suggested that the aggregation-prone protein TDP25 tagged with NLS (NLS-TDP25) can be sequestrated into the nucleolus (Fig. 1). Recently, the intranuclear quality control compartment that exists around the nucleolus was identified in *S. cerevisiae* (Miller *et al.* 2015). The nucleolus and border region with the nucleoplasm may be able to sequestrate toxic aggregation-prone proteins and prevent cellular toxicity during proteostasis dysregulation. Although penetration of TDP25 lacing NLS into the nucleolus is negatively regulated in the absence of cellular stress, a low amount of TDP25 can exist and diffuse into the nucleolus (Fig. 1 and Fig. 4). The nucleolus is known to be an important site for RNA biogenesis and performs important functions in cellular stress responses (Boulon *et al.* 2010; Audas *et al.* 2012). ActD treatment dramatically changes the environment of the nucleolus (Reynolds *et al.* 1964). In this study, ActD induced nucleolar cap-like structures with G-NLS-TDP25 and TDP43-G, but not with G-TDP25 and G-NLS^{NP}-TDP25 (Fig. 1C). TDP-43 and G-NLS-TDP25 recognize and bind to RNA containing UG repeats, while G-TDP25 and G-NLS^{NP}-TDP25 cannot (Kitamura *et al.* 2016). Therefore, formation of the nucleolar cap-like structure of TDP-43 and NLS-TDP25 may be involved in both RNA binding and the C-terminus of TDP-43 including glycine-rich region.

We recently reported that G-NLS-TDP25 can reduce cytotoxicity and the formation of cytoplasmic IBs. An important question is what is necessary to reduce the toxicity resulting from aggregation-prone TDP25. Our IP-MS and FCCS analyses showed that TDP25 interacts to HSP70, a molecular chaperone in the cytoplasm and nucleus. HSP70 prevents the aggregation of misfolded proteins and is involved in IB-sequestration of aggregation-prone proteins (Muchowski *et al.* 2000; Morimoto 2008; Kampinga & Craig 2010). Heat shock response-induced expression of heat shock proteins (e.g., HSP70, HSP90, and HSP40) plays a protective role for aggregation of TDP-43 (Chen *et al.* 2016; Lin *et al.* 2016). In particular, an inhibitor of HSP70 ATPase activity increases insoluble amount of TDP-43 and its CTF (Udan-Johns *et al.* 2014). Although the interaction between HSP70 and TDP25 has been previously reported using immunoprecipitation study (Zhang *et al.* 2010), our FCCS results directly confirmed that the specific interaction between TDP25 and HSP70 in solution occurred in an Mg^{2+}/ATP-dependent manner. The observation of HSP70 binding suggested that TDP25 exists in a misfolded state, and HSP70 chaperone cycle may play an important role for transient binding to TDP25 in cells. Moreover, co-precipitated amount of HSP70 with NLS-TDP25 was not different from that with TDP25, suggesting that HSP70 can recognize both TDP25 and NLS-TDP25 in a diluted Mg^{2+}/ATP concentration. However,

NLS-TDP25 in the nucleolus was weakly co-localized with HSP70 (Fig. 5). We thus suggested that HSP70 may recognize the different misfolded state of TDP25.

NLS-TDP25 oligomers may result in less cytoplasmic IB formation, in addition to nuclear retention *via* the NLS (Fig. 6). Our biophysical FRET and FRAP analyses revealed that NLS-TDP25 formed dynamic and ordered assemblies in the nucleolus, while the assembly state of TDP25 in the cytoplasmic IBs was disordered and immobile (Fig. 2 & 3). We recently reported that NLS-TDP25 binds to RNA containing UG repeat. The dynamic accumulation of NLS-TDP25 in the nucleolus may result from RNA binding. Poly-dipeptide sequences encoded by the ALS-associated C9orf72 repeats bind to the nucleolus and impede RNA biogenesis (Kwon *et al.* 2014). Thus, nucleolar localization of aggregation-prone proteins is not likely to be a cure-all for preventing cytotoxicity. We also recently reported that non-RNA binding NLS^{NP}-tagged TDP25 showed less nucleolar localization but lower toxicity in the cells (Kitamura *et al.* 2016). Consequently, nucleoplasmic sequestration of TDP25 may be important in reducing cytotoxicity due to its role in reducing the cytoplasmic concentrations of toxic species, and the underlying mechanism(s) of toxicity and details of the associated quality control mechanism for misfolded proteins should be investigated.

The estimated molecular weight of TDP25 from the D_{Fast} value in live cells was 103 and 186 kDa in the nucleoplasm and cytoplasm, respectively, which both exceed the molecular weight limit for passive diffusion through the nuclear pore complex (~50 kDa) (Mattaj & Englmeier 1998). A possible explanation of the nuclear-localization mechanism of TDP25 lacking a classical NLS is that TDP25 can bind to endogenous NLS-carrying proteins, and/or TDP25 may include a non-classical NLS sequence such as the acidic M9 domain of hnRNP A1 (Siomi & Dreyfuss 1995). To prevent the cytoplasm-associated cytotoxicity of TDP25, the mechanism of nuclear localization of TDP25 should be clarified.

We concluded that cytoplasmic localization of non-ordered aggregation including TDP25 may be an important role to exert toxicity; therefore, the discovery of drugs that can avoid cytoplasmic localization and stabilize the structure of non-toxic oligomers, such as NLS-tagged TDP25, should be important for the prevention and cure of ALS.

Experimental procedures

Plasmids and reagents. Plasmids for GFP-tagged TDP-43, TDP25, NLS-TDP25, and NLS^{NP}-TDP25 (TDP43-G, G-TDP25, G-NLS-TDP25, and G-NLS^{NP}-TDP25, respectively) expression were

described previously (Kitamura *et al.* 2016). NLS^{NP} means nucleoplasmin-derived NLS sequence. GFP tag was fused at N-terminus of TDP25 and NLS-TDP25, while that was fused at C-terminus of TDP-43. For FRET analysis, cDNA fragment of C-terminally fluorescent protein-tagged NLS-TDP25 was created using PCR and followed by sub-cloned into pcDNA3.1(+) (Thermo Fisher Scientific, Waltham, MA). Construction of NLS-tagged GFP and mCherry-tagged fibrillarin (G-NLS and R-fibrillarin, respectively) was described previously (Kitamura *et al.* 2015b). The HSP70 sequence in a plasmid encoding HSP70-GFP (peGFP-N1-HSP70; kindly provided from Prof. H. Kubota in Akita Univ., Akita, Japan) was subcloned into pmCherry-N1 (HSP70-R). MG-132 and actinomycin D (ActD) were purchased from Peptide Institute (Osaka, Japan) and Sigma-Aldrich (St. Louis, MO), respectively.

Cell culture and transfection. Mouse neuroblastoma Neuro2A cells were maintained at 37°C and 5% CO_2 in Dulbecco's Modified Eagle's Medium (DMEM; #D5796; Sigma-Aldrich) supplemented with 10% fetal bovine serum (FBS; GE Healthcare, Logan, UT), 100 U/mL penicillin G (Sigma-Aldrich), and 100 µg/mL streptomycin (Sigma-Aldrich). Lipofectamine 2000 (Thermo Fisher Scientific) was used for transfections, as described previously (Kitamura *et al.* 2015b; Kitamura *et al.* 2016).

Confocal fluorescence microscopy. Confocal fluorescence microscopy images were acquired on an LSM 510 META system through a C-Apochromat 40×/1.2NA Korr. UV-VIS-IR water immersion objective (Carl Zeiss, Jena, Germany). GFP was excited at 488 nm. GFP fluorescence was collected through a band-pass filter (BP505-530). Pinhole sizes were set to 72 µm. The zoom factor was set to 4×. The X- and Y-scanning sizes were each 512 pixels. Co-localization images between G-NLS-TDP25 and R-fibrillarin were acquired as previously reported (Kitamura *et al.* 2015b).

Immunofluorescence staining and super-resolution microscopy. Cells were cultivated on cover slips (0.15–0.18 mm, Matsunami, Osaka, Japan). Transfection was performed using Lipofectamine 2000 (Thermo Fisher Scientific) as described previously (Kitamura *et al.* 2015b). Cells were fixed with 4% paraformaldehyde buffered with HEPES-KOH (pH 7.5) at 37°C. The cells were washed in TBS and permeabilized in the presence of 0.5% (v/v) Triton X-100 (Nacalai Tesque, Kyoto, Japan) and 0.5% (w/v) saponin (Sigma-Aldrich). After blocking nonspecific binding activity in a blocking buffer containing 5% normal goat serum (DAKO, Glostrup, Denmark) and 20% glycerol in PBS, the cells were incubated for 1 h at room temperature in blocking buffer containing a primary antibody against enhanced GFP (EGFP) conjugated with Alexa Fluor 488 (#D153-A48; MBL, Nagoya, Japan), 1.0 µg/ml

propidium iodide (PI; Thermo Fisher Scientific) for nucleolar staining, and 1.0 μg/ml Hoechst 33342 (Sigma-Aldrich) for nucleoplasmic staining. Cells stained on cover slips were mounted with ProLong Gold (Thermo Fisher Scientific). For confocal fluorescence microscopy, images were acquired on an LSM 510 META system through a C-Apochromat 40×/1.2NA Korr. UV-VIS-IR water immersion objective (Carl Zeiss, Jena, Germany). Co-localization images in Figure 1A were acquired as previously reported (Kitamura *et al.* 2015b). For super-resolution SIM, images were acquired on an N-SIM system (Nikon, Tokyo, Japan) equipped with an Apo TIRF 100×/1.49 NA oil-immersion objective (Nikon). Alexa Fluor 488 was excited at 488 nm. Image acquisition and SIM-reconstruction were operated on an NIS-elements software platform (Nikon).

FRAP. Photobleaching experiments were performed on an LSM 510 META system through a C-Apochromat 40×/1.2NA W Korr. UV-VIS-IR objective (Carl Zeiss). GFP was excited and photobleached at 488 nm. GFP fluorescence was collected through a band pass filter (BP505-550). The pinhole size was set to 72 μm, the zoom factor was set to 5×, and the interval time for image acquisition was set to 10 s. The X- and Y-scanning sizes were each 512 pixels. The photobleaching period was 1.3 s. Relative fluorescence intensity was measured using AIM3.2 software (Carl Zeiss) and calculated according to Eq. 1.

$$\mathrm{RFI} = \frac{I_{\mathrm{BL}}(t) \cdot I'_{\mathrm{Ref}}}{I'_{\mathrm{BL}} \cdot I_{\mathrm{Ref}}(t)} \qquad [1]$$

where $I_{\mathrm{BL}}(t)$ and $I_{\mathrm{Ref}}(t)$ are the intensity at time point t in the photobleached region and the reference region, respectively. I'_{BL} and I'_{Ref} are the intensities from the same respective regions, but before photobleaching. The recovery curve for the relative fluorescence intensity was fitted to Eq. 2 in Origin 2015 software (OriginLab Corp., Northampton, MA).

$$I(t) = I_0 + Ae^{-t/k} \qquad [2]$$

where $I(t)$ is the intensity at time point t, I_0 is the base line intensity, A is the maximum recovery rate, and k is recovery constant.

Acceptor photobleaching for FRET analysis. Neuro2A cells were grown in a 35 mm glass-bottom dish (#3910-035, Asahi-Technoglass, Shizuoka, Japan) for 16 h before the transfection. A plasmid

mixture consisting of 300 ng of the plasmid encoding a donor protein (monomeric super enhanced cyan fluorescent protein; mSECFP) and 700 ng of the plasmid encoding the acceptor (mVenus or cp173mVenus) were transfected into Neuro2A cells with 2.5 μL of Lipofectamine 2000. Confocal fluorescence microscopy analysis for acceptor photobleaching was performed on an LSM 510 META through a C-Apochromat 40×/1.2NA W Korr. UV-VIS-IR objective (Carl Zeiss) at 37°C and 5% CO_2. The microscope was operated on the AIM 4.2 software platform (Carl Zeiss). mSECFP and mVenus were excited at 458 or 514 nm, respectively. The excitation beams were split by an HFT458/514 filter. CFP and Venus fluorescent signals were collected through a spectrophotometer at 477–509 and 531–649 nm, respectively. The pinhole size was set to 67 μm, the zoom factor was set to 5×, and the X- and Y-scanning sizes were 256 pixels each. The images were reconstructed using the average values from 4-line scanning. The image-acquisition and the photobleaching periods were alternately repeated until the disappearance of acceptor fluorescence. The FRET efficiency (E_{FRET}) was calculated using Eq. 3.

$$E_{\mathrm{FRET}} = 1 - \frac{I_{\mathrm{DA}}}{I_{\mathrm{D}}} \qquad [3]$$

where I_{DA} and I_{D} indicate the fluorescence intensity before and after acceptor photobleaching, respectively.

FCS. Neuro2A cells were cultured in 3.5-cm plastic dishes (Thermo Fisher Scientific) for 16 h before transfection. For expression of GFP, GFP-TDP25, GFP-NLS, and GFP-NLS-TDP25, the amount of plasmid DNA used was 200, 1000, 100, and 1000 ng, respectively. The pCAGGS plasmid was added as necessary to increase the total amount of plasmid DNA to 1.0 μg. At 24 h after transfection with Lipofectamine 2000, the culture medium was replaced, and then FCS measurements were performed. FCS measurements were performed on an LSM 510 META equipped with ConfoCor 3 system and a C-Apochromat 40×/1.2NA UV-VIS-IR Korr. water-immersion objective (Carl Zeiss), as described previously (Kitamura *et al.* 2015b). GFP was excited at 488 nm. The confocal pinhole diameter was adjusted to 70 μm. Emission signals were detected through a 505-nm long-pass filter. The fluorescence autocorrelation function, $G(\tau)$, from which the time (τ) and the absolute amount of fluorescent proteins in the detection volume were calculated, was calculated according to Eq. 4:

$$G(\tau) = \frac{\langle I(t) \cdot I(t+\tau) \rangle}{\langle I(t) \rangle^2} \qquad [4]$$

where $I(t+\tau)$ is the fluorescence intensity obtained by the single-photon counting method in a detection volume at delay time τ (angular brackets denote ensemble averages). A multicomponent diffusion model with a triplet state for curve-fitting is given by Eq. 5:

$$G(\tau) = 1 + \left[1 + \frac{T}{1-T}\exp\left(-\frac{\tau}{\tau_{\text{triplet}}}\right)\right]\frac{1}{N}\left[\sum_{i}^{m} F_i \left(1+\frac{\tau}{\tau_i}\right)^{-1}\left(1+\frac{\tau}{s^2\tau_i}\right)^{-\frac{1}{2}}\right] \qquad [5]$$

where F_i and τ_i are the fraction and diffusion time of component *i*, respectively; *N* is the average number of fluorescent molecules in the analyzed volume defined by the beam waist w_0 and the axial radius z_0; *s* is the structure parameter representing the ratio of w_0 to z_0; *m* is the number of components (m = 1 or 2); *T* is the triplet fraction; and τ_{triplet} is the relaxation time of the triplet state. $G(\tau)$ values were measured for 35 s at 37°C. After pinhole adjustment, the diffusion time and structure parameter were determined using a 10^{-7} M rhodamine 6G (Rh6G) solution as a standard before measurements. The diffusion coefficients of fluorescent molecules (D_{sample}) were calculated from the published diffusion coefficient of Rh6G, D_{Rh6G} (414 $\mu m^2 \cdot s^{-1}$) and the measured diffusion periods of Rh6G under condition (τ_{Rh6G}) and with probe proteins (τ_{sample}), according to Eq. 6:

$$D_{\text{sample}} = \left(\frac{\tau_{\text{Rh6G}}}{\tau_{\text{sample}}}\right) \cdot D_{\text{Rh6G}} \qquad [6]$$

To calculate the molecular weight, we used Eq. 7 and the diffusion coefficient of GFP in the same subcellular compartment as a standard (Kitamura *et al.* 2015b; Kitamura *et al.* 2016),

$$M_{\text{Sample}} = \left(\frac{D_{\text{Sample}}}{D_{\text{GFP}}}\right)^3 \cdot M_{\text{GFP}} \qquad [7]$$

Counts per molecule (CPM) values were determined as the mean brightness of a measured sample

divided by the number of molecules determined by FCS analysis.

Immunoprecipitation (IP) followed by MS analysis. Neuro2A cells expressing G-TDP25 or GFP were lysed in lysis buffer containing 50 mM HEPES-KOH (pH 7.5), 150 mM NaCl, 1% Triton X-100, 20% glycerol, and 1% protease inhibitor cocktail (Sigma-Aldrich). After recovery of the soluble fraction by centrifugation (15,780 × *g*, 10 min, 4°C), solutions were incubated and rotated with anti-GFP antibody-conjugated agarose beads (MBL). The beads were washed 3 times in the lysis buffer and then once in PBS. Immobilized proteins on the beads were recovered using 0.1 M glycine with HCl solution (pH 3.5). Proteins were precipitated in 10% trichloroacetic acid and washed in acetone. Dried proteins were re-solubilized and boiled in 1× Laemmli sample buffer containing 50 mM dithiothreitol, and then the samples were resolved on a 10% e-PAGEL (ATTO, Tokyo, Japan) and subjected to electrophoresis in SDS-containing buffer. Silver-stained protein bands were de-stained in a buffer containing 15 mM potassium ferricyanide and 50 mM sodium thiosulfate, after which they were dehydrated in a buffer containing 25 mM ammonium bicarbonate (ABC) and 50% acetonitrile (ACN). After reduction of disulfide bonds in a buffer containing 25 mM ABC and 50 mM Tris(2-carboxyethyl)phosphine for 10 min at 60°C, an alkylation reaction was performed in a buffer containing 100 mM 2-iodoacetamide and 25 mM ABC. The gels were washed twice in the buffer containing 25 mM ABC and 50% ACN. After the addition of 100% ACN, the gels were dehydrated. In-gel digestion was performed overnight at 30ºC, using a 10 μg/ml trypsin solution in 25 mM ABC included in In-gel trypsin digestion kit (#89871; Thermo Fisher Scientific). Recovered solutions including trypsinized peptides were dried using a vacuum evaporator centrifuge (#VEC-100, IWAKI, Shizuoka, Japan) and then solubilized in a 50% ACN solution containing 0.1% formic acid. Samples were measured using a liquid chromatography (Ultimate 3000 LC; Thermo Fisher Scientific) and mass spectrometry system (QTRAP 4000; SCIEX, Framingham, MA). The obtained peaks were analyzed using the peptide mass fingerprinting method (Perkins *et al.* 1999).

Fluorescence cross-correlation spectroscopy (FCCS). To analyze the interaction between HSP70 and TDP25, Neuro2A cells were lysed in a lysis buffer containing 50 mM HEPES-KOH (pH 7.5), 150 mM NaCl, and 1% protease inhibitor cocktail (Sigma-Aldrich). FCCS measurements were performed on an LSM 510 META equipped with the ConfoCor 3 system through a C-Apochromat 40×/NA1.2 Korr. UV-VIS-IR water-immersion objective (Carl Zeiss). GFP and RFP were excited at 488 and 594 nm, respectively. GFP and RFP fluorescent signals were separated through a NFT600 dichroic mirror.

GFP fluorescence was recorded through a BP505-540 bandpass filter. RFP fluorescence was recorded through an LP655 long-pass filter. The pinhole was set to 70 μm. The structure parameter and optical settings were adjusted using Rh6G and Alexa Fluor 594 solutions as standards. The measurement period was 90 s. Autocorrelation functions were fitted to Eq. 5. Cross-correlation functions were fitted using Eq. 8.

$$G(\tau) = 1 + \frac{1}{N}\left[\left(1 + \frac{\tau}{\tau_i}\right)^{-1}\left(1 + \frac{\tau}{s^2\tau_i}\right)^{-\frac{1}{2}}\right] \qquad [8]$$

Normalized $G_c(\tau)$ was calculated using Eq. 9.

$$\text{Normalized } G_{\mathrm{C}}(\tau) = \frac{G_{\mathrm{C}}(\tau) - 1}{G_{\mathrm{R}}(0) - 1} \qquad [9]$$

where $G_C(\tau)$ and $G_R(0)$ are the cross-correlation function and autocorrelation function of RFP at delay time zero.

Western blotting. The immunoprecipitated samples according to the procedure during IP-MS analysis were applied to a 10–20% e-PAGEL (#2331740; ATTO, Tokyo, Japan) and subjected to electrophoresis in SDS-containing buffer. The proteins were blotted on a polyvinylidene difluoride (PVDF) membrane (GE Healthcare, Logan, UT) using a mini-trans blot cell (Bio-Rad, Hercules, CA). The membranes were blocked in 5% skim milk in PBS-T (PBS containing 0.05% Tween 20). After the membranes were washed in PBS-T 3 times, a primary mouse monoclonal anti-GFP antibody (GF200; Nacalai Tesque, Kyoto, Japan), rabbit monoclonal anti-HSPA8 (#EP1531Y; Abcam, Cambridge, United Kingdom), or mouse monoclonal anti-GAPDH (#6C5; HyTest, Turku, Finland) was allowed to react with the membrane in the blocking buffer or Can Get Signal Solution 1 (TOYOBO, Osaka, Japan). As secondary antibodies, anti-mouse or rabbit IgG antibody conjugated with horse radish peroxidase (The Jackson Laboratory, Bar Harbor, ME) was incubated with the membranes in the blocking solution. Images of the luminescent signals were acquired on a LAS 4000 mini (Fujifilm, Tokyo, Japan) with an ECL reagent (GE Healthcare). The images were processed in the ImageJ 1.50i software (National Institutes of Health, Bethesda, MD) and Photoshop CS4 software (Adobe Systems, San Jose, CA).

Generation of graphs and statistics. Student's *t*-test was performed in Microsoft Excel 2013 or 2015 to determine statistical significances. Graphs were drawn using Origin 2016 (Origin Lab. Corp., Northampton, MA).

Acknowledgements

We thank the Kinjo laboratory members (especially Ms. M. Ito-Ueguchi) for providing technical assistance. We are grateful to the Nikon Imaging Center at Hokkaido University and Prof. H. Sabe (Graduate School of Medicine, Hokkaido University) for use of a super-resolution microscope (N-SIM). A.K. was supported by a Japan Society for Promotion of Science (JSPS) Grant-in-Aid for Scientific Research (C) (#26440090) and a Grant-in-Aid for Young Scientists (B) (#23770215); by a grant for Development of Systems and Technologies for Advanced Measurement and Analysis from the Japan Agency for Medical Research and Development (AMED); by a grant-in-aid of The Nakabayashi Trust for ALS Research (Tokyo, Japan); and by a grant-in-aid of Japan Amyotrophic Lateral Sclerosis Association (JALSA, Tokyo, Japan) for ALS research. A.K. and M.K. were supported by a JSPS Grant-in-Aid for Scientific Research on Priority Areas (#19058001).

Figure legends

Fig. 1 Intracellular localization of TDP25 and NLS-tagged TDP25

(A) Confocal microscopic images of fixed Neuro2A cells expressing TDP43-G, G-TDP25, or G-NLS-TDP25. The nucleolus was stained using propidium iodide (PI). Nuclear DNA was stained using Hoechst 33342. Scale bar = 10 μm. (B) Detailed localization pattern of TDP43-G, G-TDP25, and G-NLS-TDP25 in fixed Neuro2A cells using structured-illumination microscopy (SIM). Scale bar = 5 μm. (C) Subcellular confocal imaging in live Neuro2A cells, with or without treatment with 0.4 μM ActD. Scale bar = 5 μm. The white arrows indicate nucleolar cap-like structures. (D) The proportion of cells containing the nucleolar cap-like structures of TDP43-G and G-NLS-TDP25 (mean ± SD; n = 3). All quantified proportion of cells carrying this structures is represented in Supplementary Figure 1. (E) Distribution changes of nucleolar G-NLS-TDP25 (green) and R-fibrillarin (red) as nucleolar markers after treatment with 2 μM MG-132 (a proteasome inhibitor) in live Neuro2A cells. Scale bar = 5 μm. (F) The proportion of cells containing nucleolar boundary localization of expressed GFP-tagged protein

(mean ± SD; n = 3).

Fig. 2 FRAP analysis of G-NLS-TDP25 in the nucleolus

Molecular dynamics of G-NLS-TDP25 and G-NLS (negative control) in the nucleolus in live Neuro2A cells (n=4–6). The Y-axes show the relative fluorescence intensity (RFI). The dashed gray lines indicate the values of zero and 1.0 RFI. Dots and bars indicate mean ± SD. *p < 0.05, **p < 0.01, and ***p < 0.001 (Student's t test), between control and MG-132 treatment. The green and magenta lines show recovery curves in the absence and presence of proteasome inhibitor (MG-132), respectively.

Fig. 3 Intermolecular orientation of accumulated TDP25 and NLS-tagged TDP25 in live Neuro2A cells, as determined using FRET analysis

Förster/Fluorescence resonance energy transfer (FRET) efficiency of intermolecular TDP25 (magenta), NLS-TDP25 (cyan), and controls (gray). Acceptor CP (+) or (-) indicate the introduction of circularly permutated Venus (cp173mVenus) or conventional mVenus as acceptors, respectively. The numbers above the bars show the mean values. The error bars indicate the S.D. (n = 6 to 14). Student's t test; #p < 0.05 indicates comparisons to the control; *p<0.05 and **p<0.01 indicate comparisons between selected two columns. (A) FRET efficiency of N-terminally fluorescent protein-tagged TDP25 and NLS-TDP25 in IBs in the cytoplasm (Cyt.) and in the nucleolus (NL). (B) FRET efficiency of C-terminally fluorescent protein-tagged NLS-TDP25 in the nucleolus (NL). (C) FRET efficiency of N-terminally fluorescent protein-tagged TDP25 and NLS-TDP25in the cytoplasm (Cyt) and nucleoplasm (NP).

Fig. 4 Molecular dynamics of TDP25 and NLS-TDP25 in live Neuro2A cells, as determined using FCS

Fast/slow diffusion coefficients (A & B), fast/slow components (C), and counts per molecule (CPM; D) were obtained for 1- or 2-component curve fitting analysis for GFP in the nucleolus or others, respectively. Student's t test: #p < 0.05, ##p < 0.01, and ###p < 0.001 indicate significant differences compared to GFP in the same subcellular compartment; *p < 0.05 and ***p < 0.001 indicate significant differences between 2 groups.

Fig. 5 Identification of HSP70 as a TDP25-interacting partner using IP-MS and FCCS

(A) Silver-stained gel images after IP using an anti-GFP antibody. G-TDP25-specifically precipitated and MS-identified bands are shown as (i)–(iv): (i) Heat shock family A member 8 (HSPA8), a HSP70, (ii and iii) GFP-TDP25, and (iv) GFP, respectively. IgG HC and LC refer to heavy and light IgG chains, respectively. F in the molecular weight marker indicates the lowest position of electrophoresis. (B) Normalized cross-correlation functions (CCFs) from FCCS measurements. CCF amplitudes correspond to the interaction strength. TDP25/HSP70: cells expressing both GFP-TDP25 and HSP70-RFP (blue and magenta lines). G/R mix: cells expressing GFP and RFP monomers as a negative control (green and orange lines). (C) Western blotting of anti-GFP-immunoprecipitated samples and input lysates of Neuro2A cells expressing GFP, G-NLS, G-TDP25 or G-NLS-TDP25 (IP and Input, respectively) by using anti-HSPA8, GFP, and glyceraldehyde-3-phosphate dehydrogenase protein (GAPDH) antibodies. Anti-HSPA8 and GAPDH antibodies detected endogenous proteins in Neuro2A cells. The numbers in right side of the blotted image show migrated positions of molecular weight size marker. Several low molecular weight bands observed in anti-GFP-stained samples of G-TDP25 and G-NLS-TDP25 were partially cleaved products. (D) Confocal fluorescence images of living Neuro2A cells. GFP- and RFP-tagged proteins indicated in the images were transiently expressed in Neuro2A cells (green and magenta color, respectively). White arrows or arrowheads indicate the co-localized position between GFP-tagged proteins and HSP70-RFP or the position of nucleolus, respectively. Co-localization images of cells expressing TDP43-GFP or GFP and HSP70-RFP were included in Fig. S3. Scale bar = 5 μm.

Fig. 6 A model of formation of toxic- or non-toxic TDP25 aggregates/oligomers

A putative comparison of the mechanisms of oligomerization of NLS-TDP25 and TDP25. A putative structure of TDP25 was used, based on results from a previous study (Kitamura *et al.* 2016). TDP25 aggregate formation is protected by interactions with RNA (green) (Kitamura *et al.* 2016). The NLS-tag binds to nucleolar RNA (orange) (Kitamura *et al.* 2015b). Intermolecular assembly of NLS-TDP25 via nucleolar RNA may form differently ordered oligomers (bottom left). In contrast, TDP25 lacking complexed RNA immediately forms cytoplasmic aggregates (bottom right).

References:

Audas, T.E., Jacob, M.D. & Lee, S. (2012) Immobilization of proteins in the nucleolus by ribosomal intergenic spacer noncoding RNA. *Molecular Cell* **45**, 147-157.

Bacia, K., Kim, S.A. & Schwille, P. (2006) Fluorescence cross-correlation spectroscopy in living cells. *Nature Methods* **3**, 83-89.

Blokhuis, A.M., Groen, E.J., Koppers, M., van den Berg, L.H. & Pasterkamp, R.J. (2013) Protein aggregation in amyotrophic lateral sclerosis. *Acta Neuropathologica* **125**, 777-794.

Boulon, S., Westman, B.J., Hutten, S., Boisvert, F.M. & Lamond, A.I. (2010) The nucleolus under stress. *Molecular Cell* **40**, 216-227.

Brehme, M., Voisine, C., Rolland, T., Wachi, S., Soper, J.H., Zhu, Y., Orton, K., Villella, A., Garza, D., Vidal, M., Ge, H. & Morimoto, R.I. (2014) A chaperome subnetwork safeguards proteostasis in aging and neurodegenerative disease. *Cell Reports* **9**, 1135-1150.

Chen, H.J., Mitchell, J.C., Novoselov, S., Miller, J., Nishimura, A.L., Scotter, E.L., Vance, C.A., Cheetham, M.E. & Shaw, C.E. (2016) The heat shock response plays an important role in TDP-43 clearance: evidence for dysfunction in amyotrophic lateral sclerosis. *Brain* **139**, 1417-1432.

D'Ambrogio, A., Buratti, E., Stuani, C., Guarnaccia, C., Romano, M., Ayala, Y.M. & Baralle, F.E. (2009) Functional mapping of the interaction between TDP-43 and hnRNP A2 in vivo. *Nucleic acids research* **37**, 4116-4126.

Fung, G., Shi, J., Deng, H., Hou, J., Wang, C., Hong, A., Zhang, J., Jia, W. & Luo, H. (2015) Cytoplasmic translocation, aggregation, and cleavage of TDP-43 by enteroviral proteases modulate viral pathogenesis. *Cell death and differentiation* **22**, 2087-2097.

Gitler, A.D. & Shorter, J. (2011) RNA-binding proteins with prion-like domains in ALS and FTLD-U. *Prion* **5**, 179-187.

Hartl, F.U., Bracher, A. & Hayer-Hartl, M. (2011) Molecular chaperones in protein folding and proteostasis. *Nature* **475**, 324-332.

Kampinga, H.H. & Craig, E.A. (2010) The HSP70 chaperone machinery: J proteins as drivers of functional specificity. *Nature Reviews. Molecular Cell Biology* **11**, 579-592.

Kitamura, A., Inada, N., Kubota, H., Matsumoto, G., Kinjo, M., Morimoto, R.I. & Nagata, K. (2014) Dysregulation of the proteasome increases the toxicity of ALS-linked mutant SOD1. *Genes to Cells* **19**, 209-224.

Kitamura, A., Kubota, H., Pack, C.G., Matsumoto, G., Hirayama, S., Takahashi, Y., Kimura, H., Kinjo, M., Morimoto, R.I. & Nagata, K. (2006) Cytosolic chaperonin prevents polyglutamine toxicity with altering the

aggregation state. *Nature Cell Biology* **8**, 1163-1170.

Kitamura, A., Nagata, K. & Kinjo, M. (2015a) Conformational analysis of misfolded protein aggregation by FRET and live-cell imaging techniques. *International Journal of Molecular Sciences* **16**, 6076-6092.

Kitamura, A., Nakayama, Y. & Kinjo, M. (2015b) Efficient and dynamic nuclear localization of green fluorescent protein via RNA binding. *Biochemical and Biophysical Research Communications* **463**, 401-406.

Kitamura, A., Nakayama, Y., Shibasaki, A., Taki, A., Yuno, S., Takeda, K., Yahara, M., Tanabe, N. & Kinjo, M. (2016) Interaction of RNA with a C-terminal fragment of the amyotrophic lateral sclerosis-associated TDP43 reduces cytotoxicity. *Scientific Reports* **6**, 19230.

Kuo, P.H., Doudeva, L.G., Wang, Y.T., Shen, C.K. & Yuan, H.S. (2009) Structural insights into TDP-43 in nucleic-acid binding and domain interactions. *Nucleic Acids Research* **37**, 1799-1808.

Kwon, I., Xiang, S., Kato, M., Wu, L., Theodoropoulos, P., Wang, T., Kim, J., Yun, J., Xie, Y. & McKnight, S.L. (2014) Poly-dipeptides encoded by the C9orf72 repeats bind nucleoli, impede RNA biogenesis, and kill cells. *Science* **345**, 1139-1145.

Lin, P.Y., Folorunso, O., Taglialatela, G. & Pierce, A. (2016) Overexpression of heat shock factor 1 maintains TAR DNA binding protein 43 solubility via induction of inducible heat shock protein 70 in cultured cells. *Journal of neuroscience research* **94**, 671-682.

Lukavsky, P.J., Daujotyte, D., Tollervey, J.R., Ule, J., Stuani, C., Buratti, E., Baralle, F.E., Damberger, F.F. & Allain, F.H. (2013) Molecular basis of UG-rich RNA recognition by the human splicing factor TDP-43. *Nature Structural & Molecular Biology* **20**, 1443-1449.

Mattaj, I.W. & Englmeier, L. (1998) Nucleocytoplasmic transport: the soluble phase. *Annual review of Biochemistry* **67**, 265-306.

Miller, S.B., Ho, C.T., Winkler, J., Khokhrina, M., Neuner, A., Mohamed, M.Y., Guilbride, D.L., Richter, K., Lisby, M., Schiebel, E., Mogk, A. & Bukau, B. (2015) Compartment-specific aggregases direct distinct nuclear and cytoplasmic aggregate deposition. *The EMBO Journal* **34**, 778-797.

Morimoto, R.I. (2008) Proteotoxic stress and inducible chaperone networks in neurodegenerative disease and aging. *Genes & Development* **22**, 1427-1438.

Muchowski, P.J., Schaffar, G., Sittler, A., Wanker, E.E., Hayer-Hartl, M.K. & Hartl, F.U. (2000) Hsp70 and hsp40 chaperones can inhibit self-assembly of polyglutamine proteins into amyloid-like fibrils. *Proceedings of the National Academy of Sciences of the United States of America* **97**, 7841-7846.

Neumann, M., Sampathu, D.M., Kwong, L.K. *et al.* (2006) Ubiquitinated TDP-43 in frontotemporal lobar

degeneration and amyotrophic lateral sclerosis. *Science* **314**, 130-133.

Perkins, D.N., Pappin, D.J., Creasy, D.M. & Cottrell, J.S. (1999) Probability-based protein identification by searching sequence databases using mass spectrometry data. *Electrophoresis* **20**, 3551-3567.

Renton, A.E., Chio, A. & Traynor, B.J. (2014) State of play in amyotrophic lateral sclerosis genetics. *Nature Neuroscience* **17**, 17-23.

Reynolds, R.C., Montgomery, P.O. & Hughes, B. (1964) Nucleolar "Caps" Produced by Actinomycin D. *Cancer Research* **24**, 1269-1277.

Rigler, R., Mets, U., Widengren, J. & Kask, P. (1993) Fluorescence Correlation Spectroscopy with High Count Rate and Low-Background - Analysis of Translational Diffusion. *Eur Biophys J Biophy* **22**, 169-175.

Siomi, H. & Dreyfuss, G. (1995) A nuclear localization domain in the hnRNP A1 protein. *The Journal of Cell Biology* **129**, 551-560.

Udan-Johns, M., Bengoechea, R., Bell, S., Shao, J., Diamond, M.I., True, H.L., Weihl, C.C. & Baloh, R.H. (2014) Prion-like nuclear aggregation of TDP-43 during heat shock is regulated by HSP40/70 chaperones. *Human molecular genetics* **23**, 157-170.

Woerner, A.C., Frottin, F., Hornburg, D., Feng, L.R., Meissner, F., Patra, M., Tatzelt, J., Mann, M., Winklhofer, K.F., Hartl, F.U. & Hipp, M.S. (2016) Cytoplasmic protein aggregates interfere with nucleocytoplasmic transport of protein and RNA. *Science* **351**, 173-176.

Yamashita, T., Hideyama, T., Hachiga, K., Teramoto, S., Takano, J., Iwata, N., Saido, T.C. & Kwak, S. (2012) A role for calpain-dependent cleavage of TDP-43 in amyotrophic lateral sclerosis pathology. *Nature Communications* **3**, 1307.

Zhang, Y.J., Gendron, T.F., Xu, Y.F., Ko, L.W., Yen, S.H. & Petrucelli, L. (2010) Phosphorylation regulates proteasomal-mediated degradation and solubility of TAR DNA binding protein-43 C-terminal fragments. *Molecular neurodegeneration* **5**, 33.

Zhang, Y.J., Xu, Y.F., Cook, C. *et al.* (2009) Aberrant cleavage of TDP-43 enhances aggregation and cellular toxicity. *Proceedings of the National Academy of Sciences of the United States of America* **106**, 7607-7612.

Zhang, Y.J., Xu, Y.F., Dickey, C.A., Buratti, E., Baralle, F., Bailey, R., Pickering-Brown, S., Dickson, D. & Petrucelli, L. (2007) Progranulin mediates caspase-dependent cleavage of TAR DNA binding protein-43. *The Journal of neuroscience* **27**, 10530-10534.

Figure 1

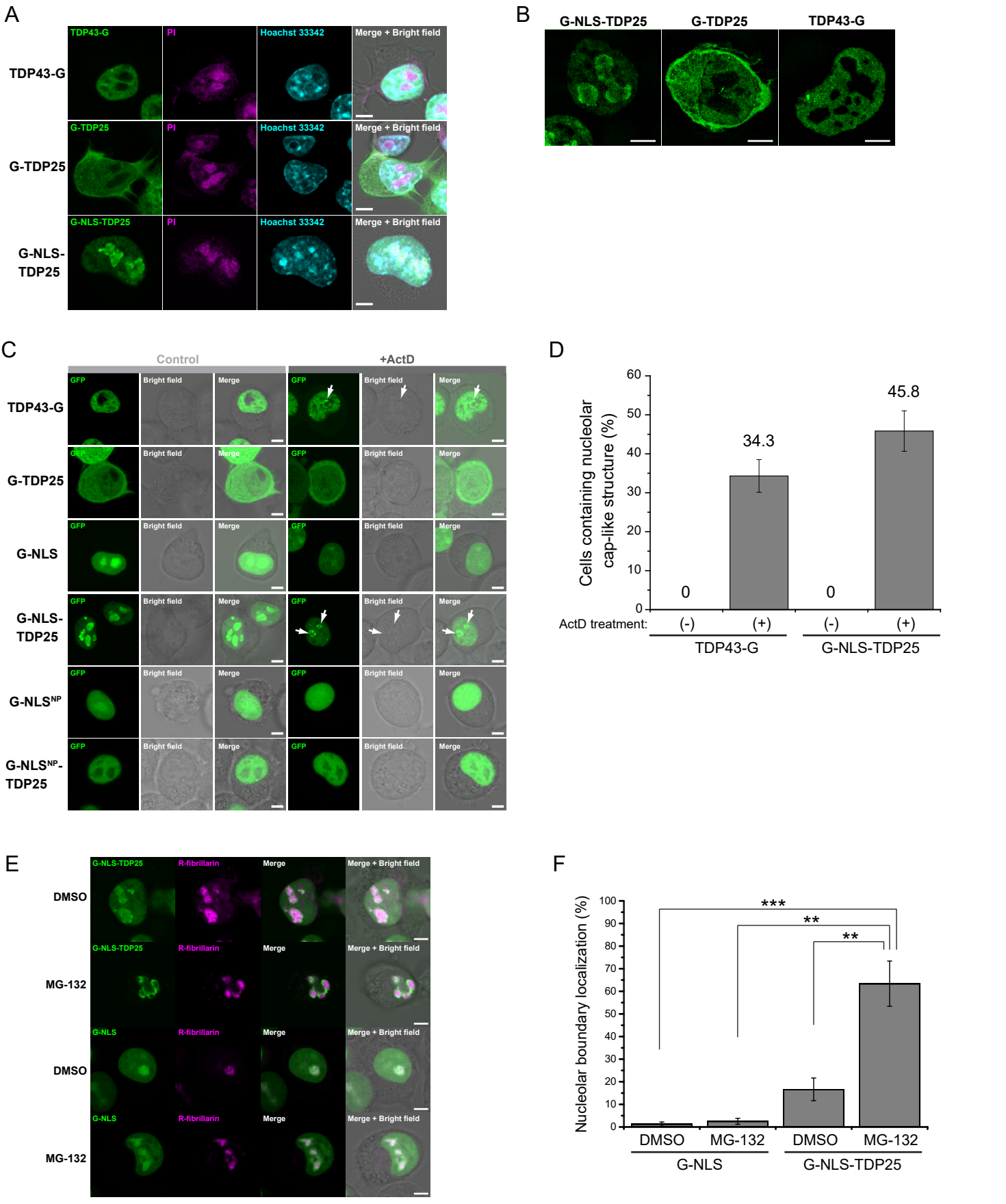
A
TDP43-G
PI
Hoachst 33342
Merge + Bright field
G-TDP25
G-NLS-TDP25
B
G-NLS-TDP25
G-TDP25
TDP43-G
C
Control
+ActD
GFP
Bright field
Merge
TDP43-G
G-TDP25
G-NLS
G-NLS-TDP25
G-NLS^NP
G-NLS^NP-TDP25
D
Cells containing nucleolar cap-like structure (%)
60
50
40
30
20
10
0
45.8
34.3
0
0
ActD treatment:
(-)
(+)
(-)
(+)
TDP43-G
G-NLS-TDP25
E
G-NLS-TDP25
R-fibrillarin
Merge
Merge + Bright field
DMSO
MG-132
G-NLS
F
Nucleolar boundary localization (%)
100
90
80
70
60
50
40
30
20
10
0
***
**
**
DMSO
MG-132
DMSO
MG-132
G-NLS
G-NLS-TDP25

Figure 2

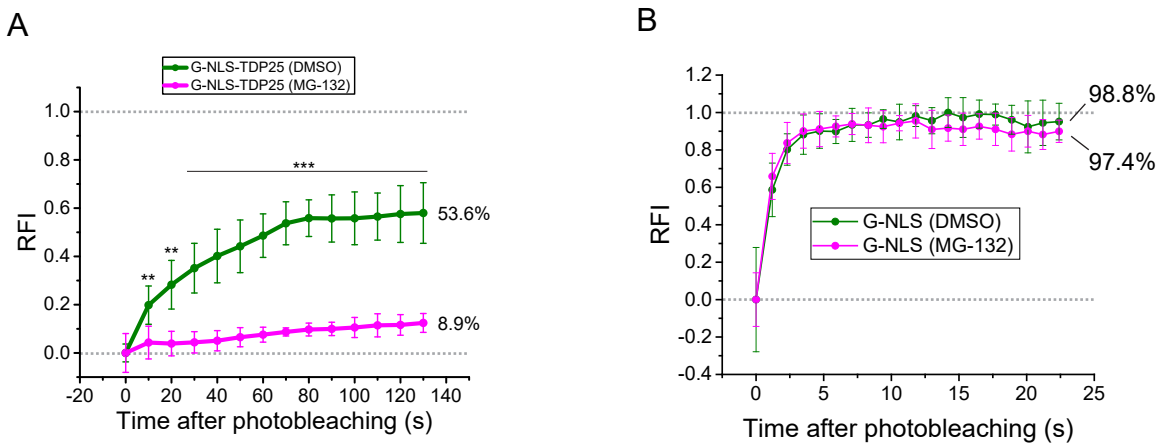
A
G-NLS-TDP25 (DMSO)
G-NLS-TDP25 (MG-132)
RFI
Time after photobleaching (s)
***
**
**
53.6%
8.9%
B
G-NLS (DMSO)
G-NLS (MG-132)
RFI
Time after photobleaching (s)
98.8%
97.4%

Figure 3

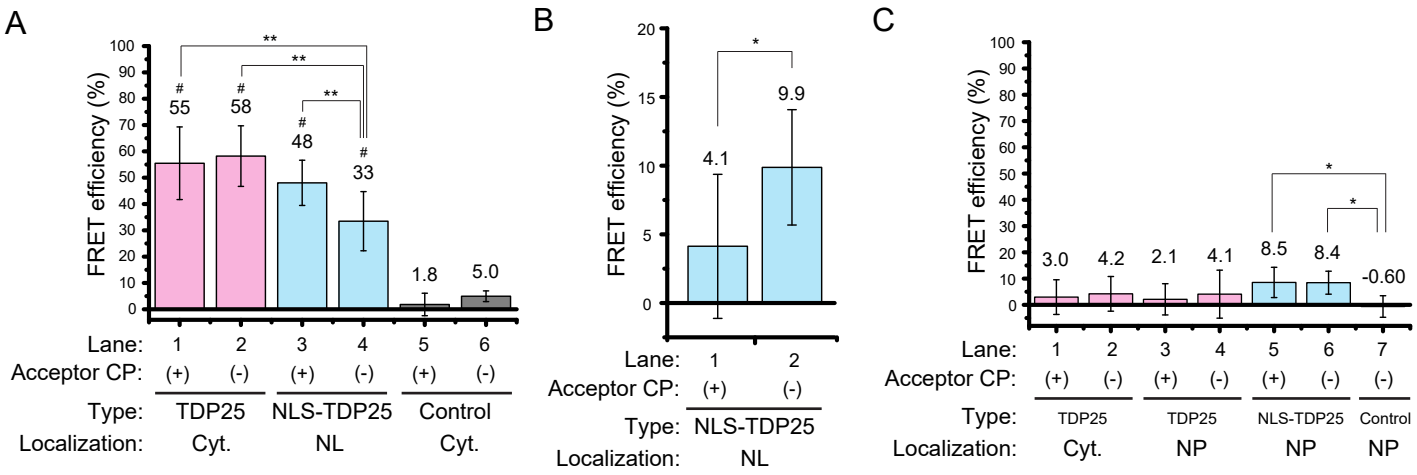
A
FRET efficiency (%)
55
58
48
33
1.8
5.0
Lane: 1 2 3 4 5 6
Acceptor CP: (+) (-) (+) (-) (+) (-)
Type: TDP25 NLS-TDP25 Control
Localization: Cyt. NL Cyt.
B
FRET efficiency (%)
4.1
9.9
Lane: 1 2
Acceptor CP: (+) (-)
Type: NLS-TDP25
Localization: NL
C
FRET efficiency (%)
3.0
4.2
2.1
4.1
8.5
8.4
-0.60
Lane: 1 2 3 4 5 6 7
Acceptor CP: (+) (-) (+) (-) (+) (-) (-)
Type: TDP25 TDP25 NLS-TDP25 Control
Localization: Cyt. NP NP NP

Figure 4

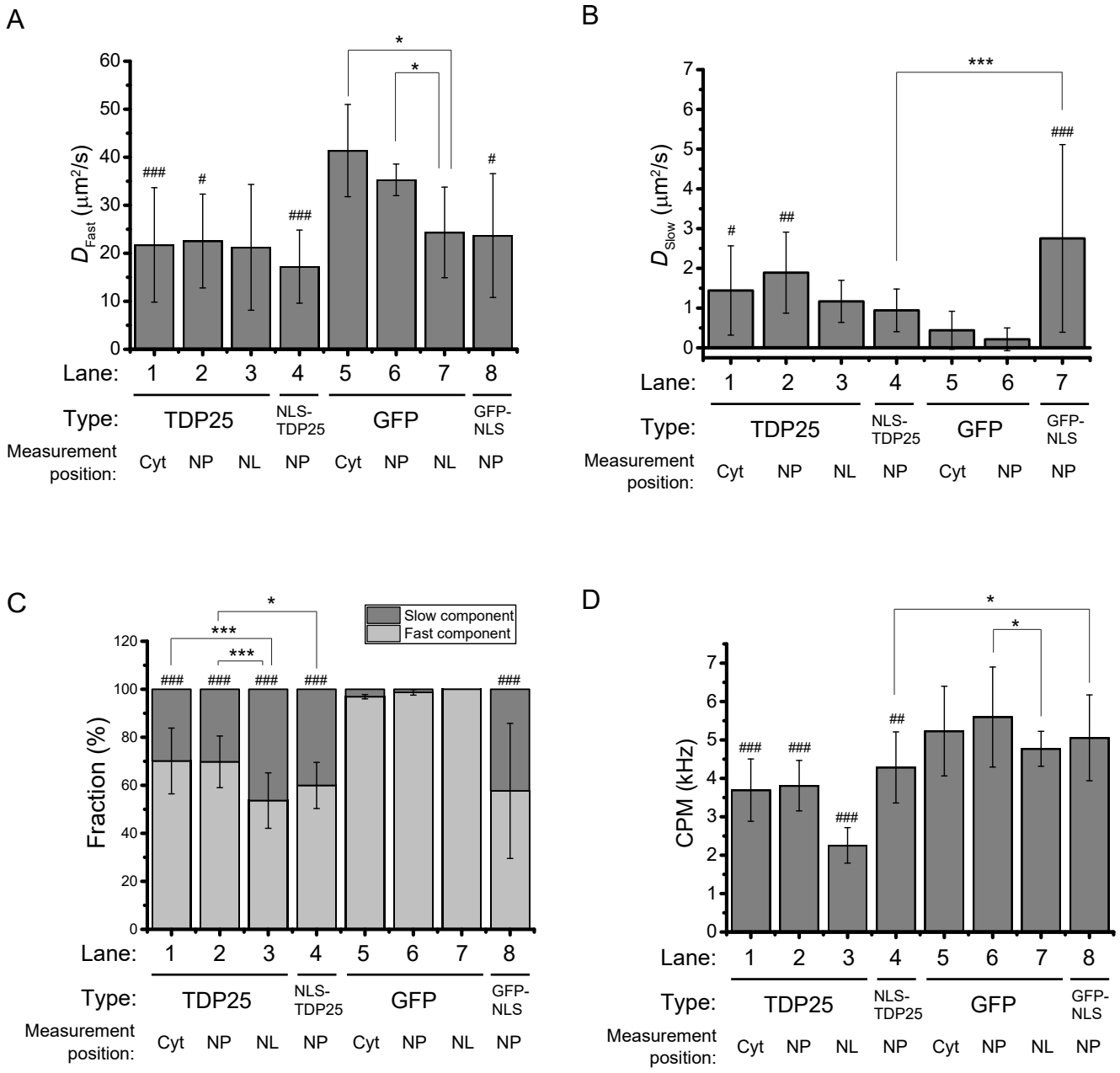
A
B
C
D
Lane:
Type:
Measurement position:
TDP25
NLS-TDP25
GFP
GFP-NLS
Cyt
NP
NL
Slow component
Fast component
Fraction (%)
CPM (kHz)

Figure 5

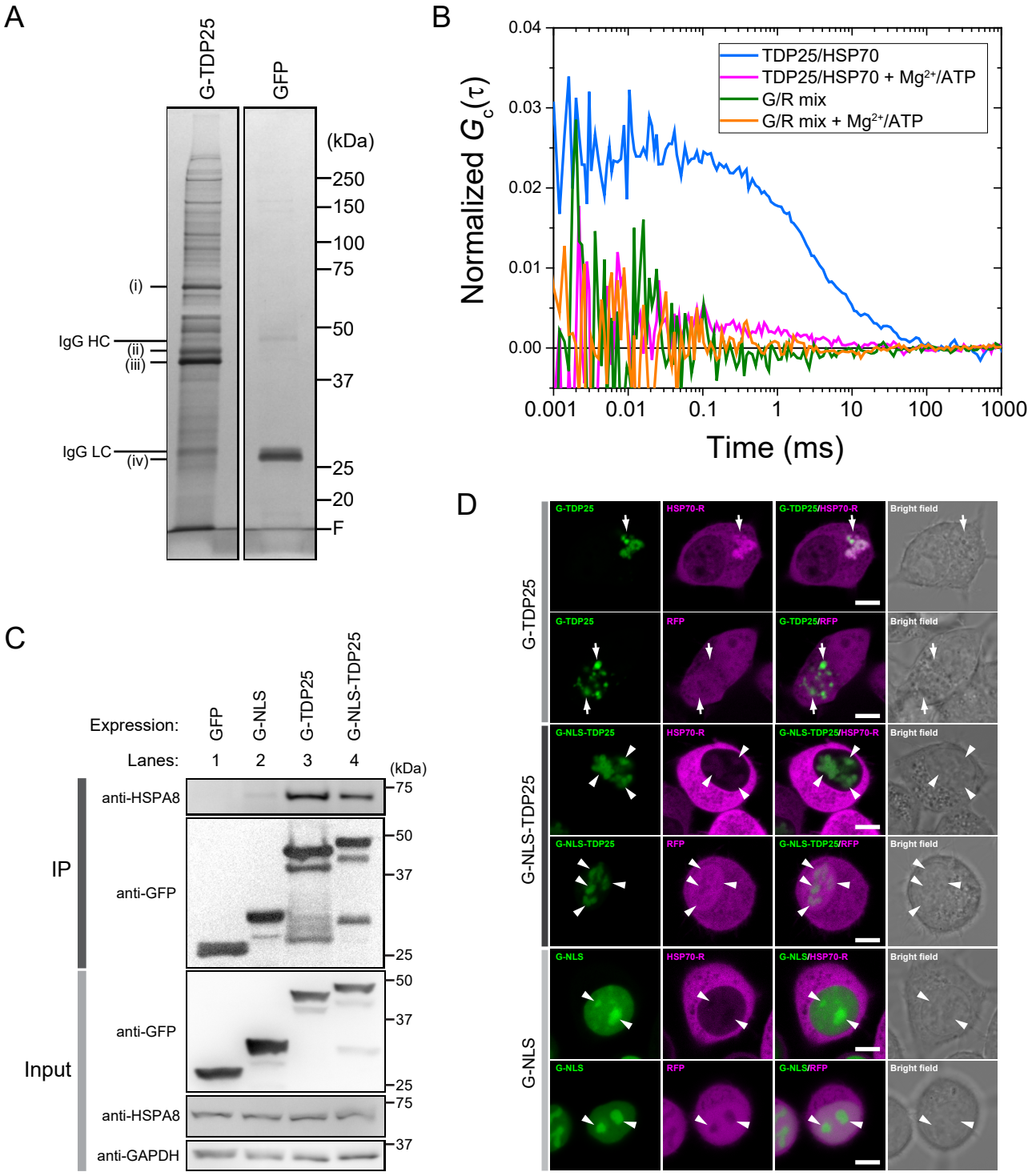
A
G-TDP25
GFP
(kDa)
250
150
100
75
50
37
25
20
F
(i)
IgG HC
(ii)
(iii)
IgG LC
(iv)
B
Normalized $G_c(\tau)$
TDP25/HSP70
TDP25/HSP70 + Mg2+/ATP
G/R mix
G/R mix + Mg2+/ATP
0.04
0.03
0.02
0.01
0.00
0.001
0.01
0.1
1
10
100
1000
Time (ms)
C
Expression:
GFP
G-NLS
G-TDP25
G-NLS-TDP25
Lanes:
1
2
3
4
(kDa)
IP
Input
anti-HSPA8
anti-GFP
anti-GFP
anti-HSPA8
anti-GAPDH
75
50
37
25
50
37
25
75
37
D
G-TDP25
G-NLS-TDP25
G-NLS
G-TDP25
HSP70-R
G-TDP25/HSP70-R
Bright field
G-TDP25
RFP
G-TDP25/RFP
Bright field
G-NLS-TDP25
HSP70-R
G-NLS-TDP25/HSP70-R
Bright field
G-NLS-TDP25
RFP
G-NLS-TDP25/RFP
Bright field
G-NLS
HSP70-R
G-NLS/HSP70-R
Bright field
G-NLS
RFP
G-NLS/RFP
Bright field

Figure 6

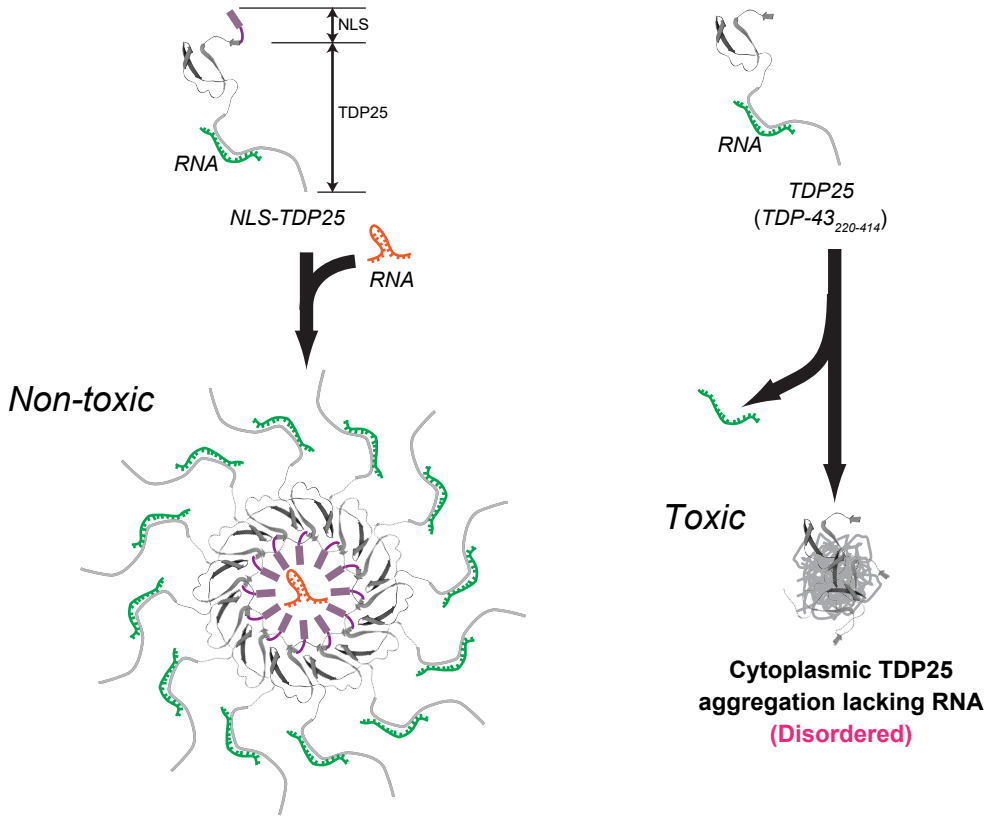

Nucleolar assembly of NLS-TDP25 *via* RNA
(Ordered)

Cytoplasmic TDP25 aggregation lacking RNA
(Disordered)